



CHORUS

This is the accepted manuscript made available via CHORUS. The article has been published as:

Dipole response of ^{238}U to polarized photons below the neutron separation energy

S. L. Hammond, A. S. Adekola, C. T. Angell, H. J. Karwowski, E. Kwan, G. Rusev, A. P. Tonchev, W. Tornow, C. R. Howell, and J. H. Kelley

Phys. Rev. C **85**, 044302 — Published 2 April 2012

DOI: [10.1103/PhysRevC.85.044302](https://doi.org/10.1103/PhysRevC.85.044302)

Dipole response of ^{238}U to polarized photons below the neutron-separation energy

S. L. Hammond, A. S. Adekola*, C. T. Angell†, and H. J. Karwowski

*Department of Physics and Astronomy,
University of North Carolina at Chapel Hill,
Chapel Hill, North Carolina 27599, USA.*

and

Triangle Universities Nuclear Laboratory, Durham, North Carolina 27708, USA.

E. Kwan‡, G. Rusev§, A. P. Tonchev‡, W. Tornow, and C. R. Howell

*Department of Physics, Duke University,
Durham, North Carolina 27708, USA.*

and

Triangle Universities Nuclear Laboratory, Durham, North Carolina 27708, USA.

J. H. Kelley

*Department of Physics, North Carolina State University,
Raleigh, North Carolina 27695, USA.*

and

Triangle Universities Nuclear Laboratory, Durham, North Carolina 27708, USA.

(Dated: March 19, 2012)

Nuclear resonance fluorescence experiments were carried out at the High-Intensity γ -ray Source facility at Triangle Universities Nuclear Laboratory to characterize the low-energy dipole structure of ^{238}U using 100% linearly-polarized photon beams from 2.0 to 6.2 MeV. One-hundred-thirteen transitions corresponding to de-excitations to the ground state in ^{238}U were observed for the first time and the energy, spin, parity, integrated cross section, reduced width, and branching ratio were determined for each of these identified levels. The total $E1$ γ -ray interaction cross section was calculated and it was deduced that the observed concentration of low-lying $E1$ transitions were excited from the low-energy tail of the giant dipole resonance and were not a pygmy dipole resonance. Comparisons were made between quasiparticle random-phase approximation calculations and the experimentally-observed strength. The observed and predicted $M1$ strength agreed well with each other. However, there was no similar agreement for the $E1$ strength.

PACS numbers: 23.20.Lv, 24.30.Gd, 25.20.Dc, 27.90.+b

I. INTRODUCTION

Much experimental effort is focused on measuring the magnetic ($M1$) and electric ($E1$) dipole strengths in nuclei [1]. Observation of dipole states are important because they characterize the various collective and single particle nuclear excitation modes, in particular, the “scissors” mode, the spin-flip mode, and the pygmy dipole resonance. These different excitation modes are prominent in various regions below or near the neutron separation energy and represent important nuclear structure phenomena. For ^{238}U , as well as for other actinide nuclei, a complete characterization below the neutron-separation energy is absent from nuclear databases.

The orbital $M1$ “scissors” mode is described as the nuclear motion in which deformed bodies of protons and neutrons vibrate against each other [2]. In this collective mode, the ground-state transition strength in actinide nuclei is generally fragmented and concentrated in the energy region below 3 MeV with considerable dependence on deformation [3]. In previous $^{238}\text{U}(\gamma, \gamma')$ experiments [4, 5], the scissors mode is observed between 2.0-2.5 MeV and the summed $M1$ strength is measured to be $\Sigma B(M1) = 3.2(2) \mu_N^2$ with a mean excitation energy ω_{M1} of 2.3(2) MeV. This $\Sigma B(M1)$ is comparable to those determined for rare-earth nuclei, where the scissors mode is observed at energies between 2.4 - 3.7 MeV with $\omega_{M1} \sim 3.0$ MeV and $\Sigma B(M1)$ between 0.20(2) - 3.7(6) μ_N^2 , depending on the degree of deformation [6]. Enders *et al.* [6] noted that $\Sigma B(M1)$ depends specifically on the square of the deformation parameter δ .

The $M1$ spin-flip mode is a collective vibration between those nucleons which undergo a spin-change and those that do not change spin [7]. This mode carries the majority of the $M1$ strength [8]. An inelastic proton-scattering experiment estimated the upper limit of the $M1$ spin-flip resonance in ^{238}U to be 15 - 25 μ_N^2 in the energy range of 4 - 10 MeV [8, 9]. However, investigations of this mode for actinide nuclei have been limited to measurements of the continuum because of the large density of states. For comparison, $\Sigma B(M1)$ has been

*Present affiliation: AREVA/Canberra Industries, Inc., Meriden, Connecticut 06450, USA.

†Present affiliation: Quantum Beam Science Directorate, Japan Atomic Energy Agency, Shirakara-Shirane 2-4, Tokai-mura, Ibaraki 319-1195, Japan

‡Present affiliation: Physics Division, Lawrence Livermore National Laboratory, Livermore, California 94550, USA.

§Present affiliation: Chemistry Division, Los Alamos National Laboratory, Los Alamos, New Mexico 87545, USA.

‡Present affiliation: Physics Division, Lawrence Livermore National Laboratory, Livermore, California 94550, USA.

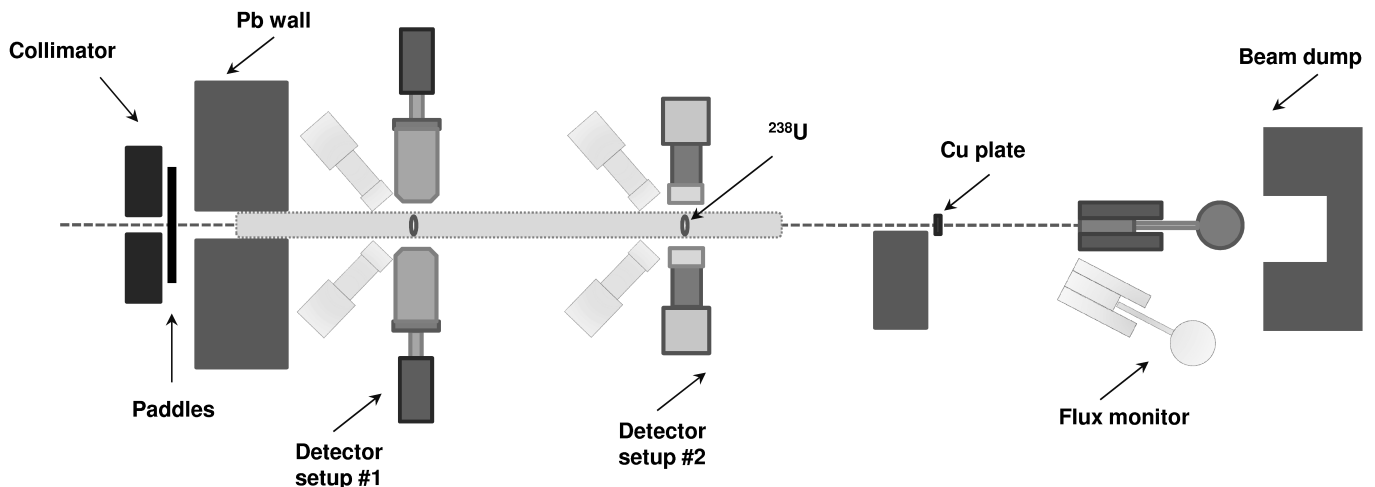


FIG. 1: The setup for (γ, γ') experiments at HI γ S for the current work (top view). All detectors were not used during data collection at each energy scan. The flux monitor detector is shown on axis as well as at the Compton scattering position of 11.2° . The figure is not drawn to scale.

found in similarly deformed rare-earth nuclei to be between $10 - 15 \mu\text{N}^2$ in the energy range of 6 - 10 MeV [10].

The pygmy dipole resonance (PDR) is comprised of a concentration of low-lying $E1$ excitations in deformed nuclei with a substantial neutron excess [11]. There have been many recent measurements of the existence of a PDR [12–14]. The origin of this $E1$ excitation is described specifically as the vibration of the neutron skin against the inert core of the nucleus. It is expected that as the neutron excess increases, so should the strength of the PDR. Furthermore, it has been suggested that the dipole strength, located at energies below or above the neutron-separation energy S_n , must be enhanced by the deformation present in the nucleus itself [15, 16].

Theoretical calculations using quasiparticle random-phase approximation (QRPA) predict substantial γ -ray strength in the energy region below the neutron separation energy from both $M1$ and $E1$ excitations in neutron-rich, deformed nuclei [17, 18]. More experimental data are needed to identify and to distinguish between the various collective modes; whether these modes are local phenomena present in only a few nuclei or whether they are global phenomena, manifesting themselves within all deformed nuclei. Theoretical calculations do agree, at least, on one point with prior experiments: in general, the density of 1^+ states decreases as the excitation energy increases, while the density of 1^- states increases with energy as it approaches the giant dipole resonance (GDR).

In recent years, it became possible to improve the sensitivity of nuclear resonance fluorescence (NRF) experiments significantly because of the availability of quasi-monenergetic, high-intensity, and linearly-polarized beams. In the NRF process, an incident γ ray excites the nucleus in its ground state, into a higher-energy state, typically populating a $\Delta J=1$ level (a $\Delta J=2$ level is much less probable). Afterward, the nucleus deexcites and if the excitation energy is below the particle-emission threshold, only γ rays are emitted, populating the ground state or lower-lying excited states. Since the momentum transfer associated with NRF is small, lower

dipole ($\Delta L=1$) excitations are highly favored over quadrupole ($\Delta L=2$) ones, making it a good probe for studying $M1$ and $E1$ excitations in nuclei.

This article describes NRF measurements on ^{238}U , performed at the High-Intensity γ -ray Source (HI γ S) facility [19] at the Triangle Universities National Laboratory (TUNL). The current work follows the NRF techniques of previous studies on ^{235}U [20] and on ^{232}Th [21], also performed at the HI γ S facility.

II. EXPERIMENT

Thirty measurements have been performed with 100% linearly-polarized photon beams with energies of 2.0-6.2 MeV and with high-intensity (total flux $\approx 2.3(1)\times 10^6 - 3.2(1)\times 10^7$ γ/s). Beams are created at the HI γ S facility through Compton backscattering of free-electron-laser photons with electrons stored in a storage ring [19]. They are collimated to have an energy spread between 3 and 5% on target. A circular lead collimator, with either 1.3 or 1.9 cm in diameter, is located ~ 60 m downstream from where the electrons collide with the free-electron-laser photons and confines the beam to a particular volume of photons per second.

As shown in Fig. 1, two detector arrays, separated by about 1.5 m, were placed downstream from the collimator and positioned around the ^{238}U targets such that the beryllium windows of the detectors were 10 cm away from the center of the target. The first array (detector setup #1) consisted of four clover detectors (each consisting of four high-purity germanium (HPGe) crystals) where each segment has $\sim 25\%$ efficiency relative to a $7.6 \text{ cm} \times 7.6 \text{ cm}$ NaI detector. The second array (detector setup #2) consisted of four HPGe detectors each with $\sim 60\%$ relative efficiency. Two more HPGe detectors with $\sim 25\%$ relative efficiency were arranged with these two arrays as well. For a polarimetry setup, the detectors were configured at one of six different spacial positions to measure

γ rays - $(\theta, \phi) = (0, \pi/2), (\pi/2, \pi/2), (\pi, \pi/2), (3\pi/2, \pi/2), (0, \pi/4),$ and $(0, -\pi/4)$, where θ is the azimuthal angle measured from the scattering plane and ϕ is the polar angle of the outgoing radiation with respect to the linearly-polarized beam (the beam direction is $+\hat{z}$ axis).

Unambiguous assignment of dipole states is an important feature of experiments involving linearly-polarized beams since beam polarization allows for straight-forward assignment of observed J^π states in even-even nuclei [22]. In the present work, γ rays corresponding to $M1$ transitions are observed predominately in the detectors placed at angles of $(0, \pi/2)$ and $(\pi, \pi/2)$ (horizontal detectors), and those corresponding to $E1$ transitions are observed in the detectors placed at angles of $(\pi/2, \pi/2)$ and $(3\pi/2, \pi/2)$ (vertical detectors). Backward detectors placed at the angles of $(0, \pi/4)$, and $(0, -\pi/4)$ are used to distinguish between $M1$ and $E2$ transitions.

A large volume (123% relative efficiency) HPGe detector was placed in the beam axis prior to NRF data collection to measure the beam energy and the energy profile of the photon beam. During the beam-energy measurement, copper-block attenuators were placed ~ 40 m upstream from the detector setup #2 to decrease the γ -ray intensity on the detector. The spectra from these measurements were unfolded using GEANT3 [23] simulations to correct for the detector response in order to determine the beam-energy profile as shown in Fig. 2. The beam attenuation by the copper blocks is a slowly-varying function with the energy in the range of 2.0 - 6.2 MeV. It is a negligible correction (less than 0.1% at $E_\gamma = 2.0$ MeV, for example) to account for the left end of the distribution of the beam as a bit larger than the right end when the beam itself is about 100 - 200 keV wide.

After the beam-energy measurement was completed, the large volume HPGe detector was moved out of the beam path and set to an angle of either $6.2(1)^\circ$ or $11.2(4)^\circ$ (with respect to the beam axis) for an absolute measurement of the photon flux. A 1.1-mm-thick copper plate was placed directly in the beam path, about 100 cm downstream from detector setup #2 and about 161 cm or 181 cm upstream from this flux monitor depending on the Compton angle chosen. Thus, the absolute beam flux on target was established during data acquisition for each beam energy using the observed Compton-scattered γ rays.

The targets consisted of depleted uranium disks, which are about 2.50(5) cm in diameter and are encased within a thin, plastic sealant. Each disk has a mass of 6.5 g with a thickness of about 0.16 cm. A target is assembled with 1, 2, or 3 disks stacked together. The number of disks chosen for a particular beam energy was carefully selected to maximize the NRF count rate while keeping the dead time below 50%. This collection of sealed ^{238}U disks was housed within an evacuated plastic tube, that extended ~ 1 m past the detector setup #2. In each measurement, the photon beam spot size was smaller than the cross-sectional area of the target.

Standard calibration sources were used to establish the efficiency $\epsilon(E_\gamma)$ for all detectors up to $E_\gamma = 3.4$ MeV. The efficiency of the flux-monitor detector was found by positioning a calibrated ^{56}Co source to the copper plate as described in Ref. [20]. MCNPX simulations [24] were carried out to extend the

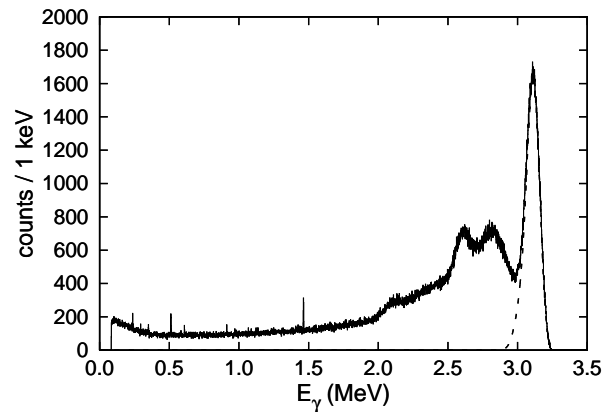


FIG. 2: Beam-energy measurement (solid histograms) with detector-response corrected beam profile overlaid (dashed curve) for $E_\gamma = 3.1$ MeV.

detector efficiency curve above $E_\gamma = 3.4$ MeV.

Natural room background peaks which are present in every spectra, namely the 1461 keV γ -ray line (^{40}K) and the 2615 keV γ -ray line (^{208}Tl), were used to calibrate the energy and calculate the dead time for all detectors. Dead time of the data-acquisition systems for the detectors was found by comparing the rate of γ rays generating the 1461 keV lines in the spectra with and without beam. From this method, the dead time [25] was determined to first order to be about 15-50% for setups #1 and #2, and about 1-3% for the flux monitor.

III. DATA ANALYSIS

The summed spectra from the $^{238}\text{U}(\gamma, \gamma')$ measurements in the horizontal, vertical, and backward-angle detectors are plotted in Fig. 3 for $E_\gamma = 2359$ keV and in Fig. 4 for $E_\gamma = 4210$ keV with the beam profile overlaid. Ground-state transitions are present within the beam-profile distribution, while transitions to the first-excited-state can be found inside and outside of it.

The ground-state decay widths, Γ_0 , are determined from the following equation:

$$\frac{\Gamma_0^2}{\Gamma} = \frac{I_s}{g} \left(\frac{E_\gamma}{\pi \hbar c} \right)^2, \quad (1)$$

where Γ is the total level width, I_s is the integrated cross section, g is the spin factor $(2J+1)/(2J_0+1)$, J_0 is the ground-state spin, J is the excited-state spin, and E_γ is the energy of the de-exciting γ ray.

The energy-integrated cross section I_s is calculated by using experimental observables:

$$I_s = \frac{N}{n_t \epsilon(E_\gamma) W(\theta, \phi) N_\gamma}, \quad (2)$$

where N is the dead-time-corrected number of counts in the full energy peak, and n_t is the number of target nuclei per unit area such that

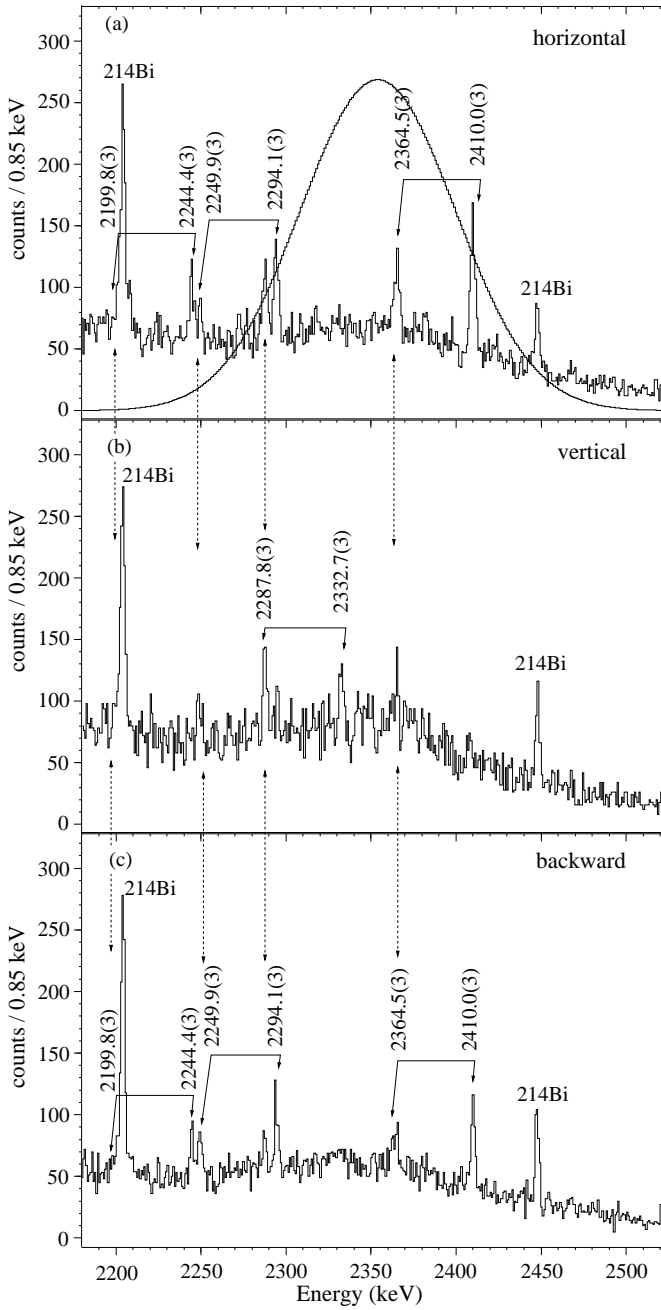


FIG. 3: NRF spectra from a ^{238}U target using an incident photon beam of $E_\gamma = 2359 \pm 103$ keV. (a) The spectrum in the horizontal detectors with the beam profile (solid curve) overlaid. (b) The spectrum in the vertical detectors. (c) The spectrum in the backward-angle detectors. Deexcitations from levels to their associated ground state and first excited state are labeled with solid arrowed lines. Transitions to the first excited state are observed in multiple detectors and are denoted by dashed lines.

$$n_t = \frac{d\rho}{A_r} N_A, \quad (3)$$

where d is the thickness of the target, ρ is the density of the target material, A_r is the atomic weight, and N_A is Avogadro's number. The quantity I_s is corrected for self-absorption [26]

and the extent of the correction depended on the individual transition being assessed.

The factor $W(\theta, \phi)$ describes the angular distribution of the γ rays following the spin sequence $J_0^\pi \rightarrow J^\pi \rightarrow J_0^\pi$ with the following combinations: $0^+ \rightarrow 1^+ \rightarrow 0^+$ or $2^+ (M1)$, $0^+ \rightarrow 1^- \rightarrow 0^+$ or 2^+ , ($E1$), and $0^+ \rightarrow 2^+ \rightarrow 0^+$ ($E2$).

To obtain the photon flux N_γ on the target, the number of counts in the scattered peak N_c is normalized by the Compton-scattering cross section,

$$N_\gamma = \frac{N_c}{\epsilon(E_\gamma)\sigma_c(E_\gamma, \theta_c)W(\theta, \phi)n_{Cu}}, \quad (4)$$

where $\sigma_c(E_\gamma, \theta_c)$ is the Compton-scattering cross section, θ_c is the Compton-scattering angle, and n_{Cu} is the areal density of the copper atoms. The quantity N_γ deduced from Compton scattering was verified within 5% with values obtained using the known resonances in the $^{11}\text{B}(\gamma, \gamma')$ reaction [16, 20, 27].

The recommended condition that all observed states must either be at or above a 2σ detection limit DL was used in order to assess the existence of the dipole transitions measured by this experiment. The detection limit is quantitatively defined

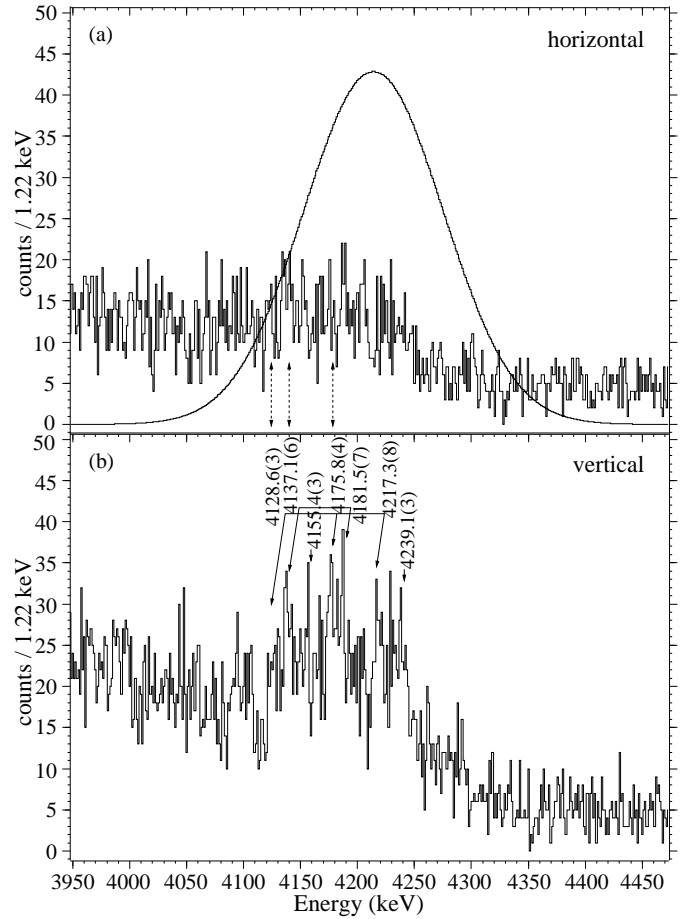


FIG. 4: NRF spectra from the ^{238}U target at an incident beam energy of 4210 keV. The histograms in a) and b) are the same as in Fig. 3. The beam distribution is shown on the top panel.

in Ref. [28] as:

$$DL = 5.4 + 3.3 \sqrt{2N_B}, \quad (5)$$

where N_B is the integral over the background with length of 2σ such that σ is the dispersion of a Gaussian fit of the peaks observed at the same energy. One example of the minimal detectable I_s (solid curve) is shown in Fig. 5 as compared to the measured I_s (solid points) for $E_\gamma = 3.1$ MeV. For the present work, the lowest detectable I_s was about 3 eVb. However, the detection limit will vary with incident beam energy, intensity, and duration of measurement.

Despite the choice of a 2σ detection limit, many peaks that were reported from the present experiment were at or above a 3σ limit, particularly 30 out of 34 $M1$ transitions and 78 out of 90 $E1$ transitions to the ground state. Therefore, a quantitative description of whether the result was obtained by coincidence or not, is needed. The statistical significance α_s is defined in terms of the error function such that [29]

$$\alpha_s = 1 - \text{erf}\left(\frac{n}{\sqrt{2}}\right), \quad (6)$$

where n is the number of standard deviations above the 2σ detection limit. A value of $\alpha_s \leq 10\%$ describes the results as a likely coincidence. About 71% and 77% of the observed $M1$ and $E1$ transitions, respectively, could be described as "very likely".

The most probable states excited in the present NRF experiment are those with $J^\pi=1^\pm$. It follows that deexcitations to states with either $J^\pi=0^+$ or 2^+ are primarily observed. The reduced transition probabilities for dipole strengths are the only ones of consequence for this work. These strengths are deduced using

$$B(\Pi L, E) \uparrow = g\Gamma_0 \sum_{\Pi L=1}^{\infty} \frac{(\hbar c/E_\gamma)^{2L+1}}{8\pi(L+1)} L[(2L+1)!!]^2, \quad (7)$$

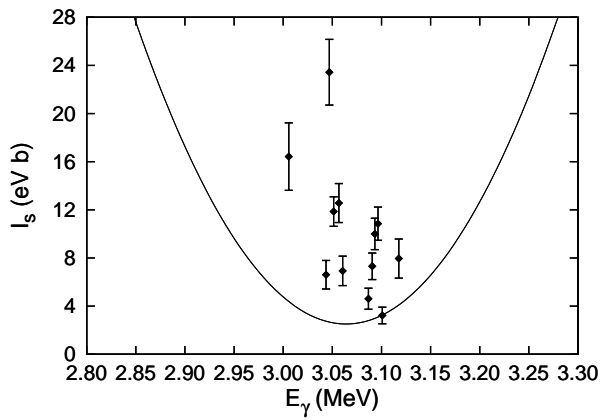


FIG. 5: The comparison of the minimal detectable I_s (solid curve) with the experimental values (\blacklozenge) for I_s at $E_\gamma = 3.1$ MeV. The detection limit varies with energy.

where orbital angular momentum $L = 1$ for dipole transitions, and Π is M for magnetic radiation and E for electric radiation. No transitions to any states other than the first excited $J^\pi = 2^+$ state at $E_x = 45$ keV are observed in the present work. Therefore, Γ can be assumed to be equal to $\Gamma_0 + \Gamma_1$, where Γ_1 is the width of transition to this 2^+ state. The experimental branching ratio can then be defined as

$$R_{exp} = \frac{\Gamma_1 \left(\frac{E_0}{E_1}\right)^3}{\Gamma_0}, \quad (8)$$

where E_1 is the energy of a branching transition to the 2^+ state while E_0 is the energy of the ground-state transition. The quantity R_{exp} is also described as the ratio of the reduced transition probabilities B of the transitions to the first excited state and to the ground state. Given this definition, the Alaga rules [30, 31] assert that, for a dipole state,

$$\begin{aligned} R &= \frac{B(1^\pi \rightarrow 2^+)}{B(1^\pi \rightarrow 0^+)} \\ &= \frac{\left| \sqrt{2J_f + 1} \langle J_f, K_1, L, K - K_1 | J, K \rangle \right|^2}{\left| \sqrt{2J_0 + 1} \langle J_0, K_0, L, K - K_0 | J, K \rangle \right|^2} \\ &= \begin{cases} 1/2 & \text{for } K=1 \\ 2 & \text{for } K=0 \end{cases}, \end{aligned} \quad (9)$$

where π is the parity of the state and K is the rotational quantum number. For dipole states, only transitions from states with $K = 0, 1$ are allowed. Values of R between $1/2$ and 2 can indicate K -mixing or a transition from a level which violates the Alaga rules.

Finally, the difference between the transition intensities for the horizontal and vertical detector orientations for each beam energy can be quantified. In general, this asymmetry A_{HV} is defined as

$$A_{HV} = \frac{I_{\gamma H} - I_{\gamma V}}{I_{\gamma H} + I_{\gamma V}}, \quad (10)$$

where $I_{\gamma H}$ ($I_{\gamma V}$) is the dead-time corrected γ -ray transition intensity in the horizontal (vertical) orientation. For a point-size detector and target, a pure $M1$ transition would have $A_{HV} = 1$ and a pure $E1$ transition would have $A_{HV} = -1$. For real detectors with finite geometry, the observed range is $-1 < A_{HV} < 1$. In order to compare values of A_{HV} across different beam energies, the asymmetry needs to be normalized by I_s producing a weighted asymmetry \bar{A}_{HV} such that

$$\bar{A}_{HV} = \frac{\sum_{i=1}^M \frac{I_{\gamma H} - I_{\gamma V}}{I_{\gamma H} + I_{\gamma V}} \cdot I_s}{\sum_{i=1}^M I_s} = \frac{\sum_{i=1}^M \left(\frac{I_{\gamma H} - I_{\gamma V}}{n_i N_\gamma} \right)_i}{\sum_{i=1}^M \left(\frac{I_{\gamma H} + I_{\gamma V}}{n_i N_\gamma} \right)_i}, \quad (11)$$

where it is assumed that the average $W(\theta, \phi)$ is similar for the entire set of M energy bins over the energy interval investigated. Each sum is over the entire set of bins involved in

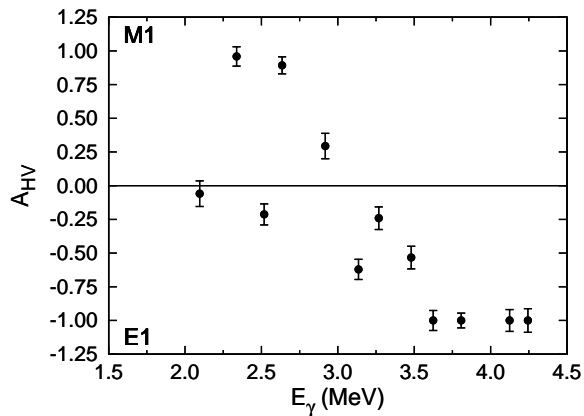


FIG. 6: The asymmetry A_{HV} for the discrete transitions in the energy range between $E_\gamma=2.0$ - 4.2 MeV. Each point indicates an average over a 0.2 -MeV energy bin.

the asymmetry comparison. For example, the denominator is the sum of all I_s for both the horizontal and vertical detectors within the energy range from the lowest energy to the highest energy being compared. This normalization is necessary since multiple choices of target mass and N_γ were used for each beam energy.

IV. RESULTS

Many discrete $M1$ and $E1$ transitions to the ground state were observed between 2.0 and 4.2 MeV. The ratio of the

$M1$ and $E1$ transition intensities is shown in Fig. 6 as averages over 0.2 -MeV wide energy bins. The transition intensities are from the discrete transitions only. When the asymmetry is close to zero, there is an equal amount of cross-section weighted transition strength from both the magnetic and electric dipole radiations at that particular beam energy. Above $E_\gamma = 4.2$ MeV, the level density becomes too large to observe individual deexcitations.

Listed in Tables I and II are the measured γ -ray energies and transition strengths of 113 newly observed transitions (27 are $M1$ and 86 are $E1$) along with eight previously measured transitions (seven $M1$ [4, 32] and one $E1$ [33]). All values are listed with their statistical uncertainties. Most of the transitions to the ground state are accompanied by transitions to the first excited state. This observation provides evidence that they are indeed NRF from ^{238}U . However, for 23 of the measured states (eight $M1$ and fifteen $E1$), no accompanying transition to the first excited state was observed above the detection limit.

Additionally, for two $M1$ and 23 $E1$ levels, both a transition to the ground state and to the first excited state are observed at the same energy. Since the angular distribution for a branching transition following the spin combination $0^+ \rightarrow 1^\pm \rightarrow 2^+$ is isotropic, then the observed intensity in the horizontal and vertical detectors will be the same. The counts of the peak associated with the first excited-state transition within the detector orientation that does not have an overlapping ground-state transition can be subtracted from the peak within the detector orientation that does have it. Therefore, the ground-state transition can be deduced as a separate entity.

TABLE I: The energies, integrated cross sections, ground-state widths, experimental branching ratios, γ -ray strengths, and the numbers of standard deviations above the 2σ detection limit of the observed magnetic dipole transitions from $J^\pi = 1^+$ states in ^{238}U . Statistical errors are shown with the values.

E_γ (keV)	I_s (eVb)	Γ_0^2/Γ (meV)	R_{exp}	$B(M1)$ (μN^2)	n	E_γ (keV)	I_s (eVb)	Γ_0^2/Γ (meV)	R_{exp}	$B(M1)$ (μN^2)	n
2017.7(4)	2.6(6)	1.5(3)	2.0(5)	0.14(5)	2	2932.6(6)	2.8(6)	2.5(5)	1.5(4)	0.06(2)	1
2079.3(4) ^{a,b,c}	6(1)	2.4(5)	0.0(1)	0.07(2)	2	2951.2(3)	6.8(5)	5.7(5)	0.9(1)	0.12(2)	2
2175.8(3) ^b	40(2)	24(1)	0.57(3)	0.96(8)	17	2963.9(8) ^a	2.2(5)	1.8(4)	0.0(1)	0.02(1)	1
2208.8(3) ^b	29(2)	18(1)	0.22(8)	0.7(1)	4	3014.5(3)	4.5(8)	3.9(7)	0.4(1)	0.05(2)	2
2244.4(3) ^b	27(2)	14.2(8)	0.15(1)	0.41(3)	7	3030.6(3) ^a	7.3(7)	6.2(6)	0.0(1)	0.06(1)	5
2294.1(3) ^b	6.6(9)	4.0(5)	1.09(6)	0.18(3)	3	3037.7(3)	7(1)	7(1)	1.2(2)	0.15(3)	3
2410.0(3) ^b	18(2)	11(1)	1.8(1)	0.61(7)	4	3042.5(6) ^a	24(6)	22(6)	0.0(1)	0.20(4)	0
2467.8(5) ^{a,b}	80(8)	48(5)	0.0(1)	0.83(8)	5	3135.0(3)	5.1(9)	4.9(8)	0.9(3)	0.08(3)	2
2499.4(3)	32(2)	20(1)	0.50(5)	0.48(4)	9	3153.7(3)	5.0(6)	4.8(6)	0.39(5)	0.08(2)	4
2638.3(3)	10(1)	7.3(7)	1.4(1)	0.25(3)	10	3172.9(3) ^f	1.9(3)	2.0(3)	1.1(1)	0.06(1)	2
2647.3(8)	25(2)	18(1)	0.84(8)	0.46(5)	20	3217.6(6)	2.6(5)	2.5(5)	0.6(2)	0.03(1)	1
2702.2(3) ^a	16(2)	10(1)	0.0(1)	0.14(2)	5	3234.5(7)	3.8(8)	4.1(8)	1.7(4)	0.09(3)	2
2738.9(9)	11(3)	8(2)	1.5(5)	0.3(1)	1	3307.3(3) ^f	9(1)	10(1)	0.6(2)	0.11(4)	5
2756.4(3) ^{a,d,e}	7(2)	5(1)	0.0(1)	0.06(1)	2	3348.3(3)	6.3(8)	13(2)	2.0(2)	0.23(4)	3
2773.0(3)	8(1)	6(1)	1.1(3)	0.16(5)	4	3366.0(5)	6(1)	8(1)	0.55(6)	0.08(2)	4
2816.8(4) ^a	26(5)	19(4)	0.0(1)	0.22(4)	2	3448.3(6)	4(1)	5(1)	1.1(1)	0.07(2)	1
2881.4(5)	2.8(6)	2.3(5)	1.4(3)	0.06(2)	2	3460.7(3)	6.4(8)	8(1)	0.58(7)	0.07(1)	4

^a No observed transition to the first excited state.

^b Previously-observed state.

^c Uncertainty of previously measured width $\Gamma_0 = 5(5)$ meV [32] is reduced to $2.4(5)$ meV.

^d Previously measured at $E_\gamma = 2754$ keV with $\Gamma_0 = 0.08$ meV [33]. New width is $\Gamma_0 = 5(1)$ meV.

^e New parity assignment for previously-observed state.

^f Both a transition to the ground state and to the first excited state are observed at this energy.

Note: the $M1$ transition at $E_\gamma = 3253$ keV ($\Gamma_0 = 0.52(19)$ meV) [33, 34] is not observed in this experiment.

TABLE II: The energies, integrated cross sections, ground-state widths, experimental branching ratios, γ -ray strengths, and the numbers of standard deviations above the 2σ detection limit of the observed electric dipole transitions from $J^\pi = 1^-$ states in ^{238}U . Statistical errors are shown with the values.

E_γ (keV)	I_s (eVb)	Γ_0^2/Γ (meV)	R_{exp}	$B(E1) \times 10^{-3}$ ($e^2\text{fm}^2$)	n	E_γ (keV)	I_s (eVb)	Γ_0^2/Γ (meV)	R_{exp}	$B(E1) \times 10^{-3}$ ($e^2\text{fm}^2$)	n
1996.7(3)	7.0(8)	2.8(3)	0.19(2)	1.2(2)	8	3470.7(3)	7(2)	9(2)	0.3(3)	0.8(8)	0
2080.7(4)	14(2)	8(1)	1.6(2)	6(1)	5	3475.2(3)	7(2)	10(2)	0.6(3)	1.1(7)	0
2093.3(4) ^{a,b}	7(1)	3.1(6)	0.0(1)	1.0(2)	3	3479.0(3)	12(1)	14(1)	0.45(9)	1.4(3)	3
2145.6(3) ^{a,b}	8(1)	3.6(6)	0.0(1)	1.1(2)	3	3489.0(3)	13(4)	24(7)	1.5(6)	4(2)	0
2332.7(3) ^c	10(2)	5.4(9)	1.4(1)	2.6(5)	4	3500.5(3) ^{a,d}	14(2)	16(2)	0.0(1)	1.1(1)	7
2365.6(3) ^a	44(6)	23(3)	0.0(1)	5.1(7)	5	3509.1(9)	12(3)	18(4)	0.7(2)	2.0(7)	1
2422.8(3) ^a	12(1)	6.2(7)	0.0(1)	1.2(1)	7	3528.0(4) ^a	4.8(7)	5.5(8)	0.0(1)	0.36(5)	4
2491.5(5)	9(1)	5.2(8)	0.7(3)	1.6(8)	5	3548.0(6) ^d	5.7(8)	7(1)	2.0(3)	1.3(3)	5
2529.0(3)	12(2)	7(1)	0.3(1)	1.8(5)	5	3562.8(3) ^d	5.4(6)	6.8(8)	1.3(3)	0.9(2)	6
2593.7(6)	6.6(7)	4.1(4)	0.18(4)	0.8(2)	9	3594.9(5) ^d	6.4(8)	8(1)	1.2(2)	1.1(2)	6
2602.5(4)	3.1(3)	1.9(2)	0.4(1)	0.4(1)	10	3608.7(3)	12(1)	14(1)	0.50(8)	1.3(2)	8
2844.2(9) ^a	3.5(5)	2.6(4)	0.0(1)	0.33(4)	5	3615.9(3) ^d	3.7(5)	5.1(7)	2.6(5)	1.0(2)	4
2862.2(5) ^d	4.3(5)	3.6(4)	1.5(3)	1.1(2)	6	3623.9(3) ^d	3.4(4)	4.5(6)	1.5(3)	0.6(1)	5
2877.1(3) ^a	4.1(6)	3.1(4)	0.0(1)	0.37(6)	2	3640.1(3)	3.5(6)	4.5(7)	0.8(2)	0.5(1)	2
2896.6(3)	5.4(8)	4.4(6)	0.8(2)	0.9(3)	4	3650.5(3)	8.2(9)	11(1)	0.9(1)	1.1(2)	7
2908.9(3)	7.5(9)	6.2(8)	0.8(2)	1.3(3)	5	3659.7(6)	3.5(5)	4.4(7)	0.7(1)	0.4(1)	3
2910.0(4)	11(1)	11(1)	1.1(1)	2.6(4)	9	3673.7(6)	4.1(7)	5.8(9)	2.0(4)	1.0(3)	3
3005.9(4) ^d	6.2(7)	5.8(6)	0.7(8)	1.0(2)	3	3728.0(9)	4(1)	5(1)	0.9(3)	0.5(2)	0
3018.9(3)	2.9(6)	2.6(5)	1.0(3)	0.6(2)	1	3738.5(8)	13(2)	18(2)	0.8(2)	1.7(5)	4
3043.6(3) ^d	5.0(6)	4.4(5)	0.1(9)	0.40(7)	3	3759.9(3) ^d	16(2)	23(2)	0.9(2)	2.3(5)	9
3046.9(3) ^{a,d}	5.0(6)	22(3)	0.0(1)	2.2(3)	7	3805.1(3) ^{b,e}	18(2)	26(2)	0.9(1)	2.5(4)	9
3051.7(3) ^d	7.8(7)	7.2(6)	0.7(1)	1.4(2)	5	3819.0(6)	11(1)	16(2)	1.1(2)	1.9(4)	7
3057.1(4) ^d	15(2)	14(1)	0.03(1)	1.9(2)	2	3828.7(3) ^a	5.2(8)	7(1)	0.0(1)	0.36(5)	3
3060.6(3)	7(1)	7(1)	0.58(5)	1.1(2)	3	3965.7(4)	10(2)	18(3)	0.49(4)	1.2(2)	3
3086.7(4)(3)	4.8(9)	4.5(9)	0.29(3)	0.6(1)	2	3990.7(9)	4.7(4)	9.5(8)	1.2(1)	0.9(1)	0
3091.0(4)	8(1)	7(1)	0.24(2)	0.9(1)	4	3995.8(3)	6(1)	11(2)	0.6(4)	0.8(1)	1
3094.2(3)	7.2(8)	7.8(7)	1.4(2)	1.8(2)	3	4023.7(7) ^d	5(1)	10(2)	1.0(1)	0.9(2)	2
3096.4(3)	11(1)	13(2)	1.1(3)	2.8(4)	6	4031.4(7)	7.5(8)	15(2)	0.5(1)	1.2(3)	2
3101.7(4)	3.8(7)	3.7(7)	0.65(6)	0.6(2)	0	4046.7(3) ^d	5.0(8)	11(2)	1.3(4)	1.0(4)	3
3117.7(4)	8(2)	9(2)	1.0(1)	1.7(4)	2	4065.3(3)	3.8(7)	9(2)	1.7(4)	1.1(3)	2
3207.8(4)	2.8(5)	2.8(6)	0.42(6)	0.5(1)	0	4072.1(6)	8(1)	14(2)	0.6(1)	1.0(2)	5
3239.6(3)	3.6(8)	4.0(9)	2.6(7)	1.2(4)	1	4088.9(7)	3.3(5)	7(1)	1.0(3)	0.6(2)	3
3274.4(3)	7(1)	9(2)	0.9(1)	1.5(3)	3	4093.4(3) ^d	8.4(7)	15(2)	0.40(4)	0.9(1)	8
3297.2(4) ^a	6(1)	7(1)	0.0(1)	0.53(9)	3	4100.2(3) ^d	4.1(4)	10(1)	1.8(2)	1.2(2)	6
3303.6(3)	2.5(4)	3.5(5)	1.1(1)	0.6(1)	3	4105.2(3) ^{a,d}	3.9(5)	6.5(8)	0.0(1)	0.27(3)	5
3329.1(6)	7(1)	9(1)	0.89(9)	1.4(2)	5	4122.9(5)	3.7(9)	7(2)	0.84(9)	0.6(2)	1
3384.3(3)	10(2)	13(2)	0.43(5)	1.4(3)	4	4138.9(7) ^d	5.2(6)	10(1)	0.41(7)	0.5(1)	4
3397.9(8) ^d	10(1)	12(2)	0.38(4)	1.3(2)	5	4145.8(3)	2.7(5)	6(1)	0.6(6)	0.7(1)	0
3416.0(4)	2.7(6)	12(2)	4.0(4)	2.0(5)	2	4151.3(6)	3.3(9)	7(2)	1.0(3)	0.5(2)	1
3421.5(5) ^{a,d}	3.0(6)	3.5(6)	0.0(1)	0.25(5)	3	4155.4(3) ^a	12(2)	20(4)	0.0(1)	0.8(2)	1
3441.0(9)	6(1)	6(1)	0.5(2)	0.7(2)	1	4175.8(4) ^d	11(2)	21(3)	0.28(3)	1.1(2)	3
3454.1(4)	3(1)	7(2)	2.6(3)	1.8(6)	0	4181.5(7)	7(1)	16(3)	1.0(1)	1.2(3)	2
3467.8(6) ^d	9(1)	10(1)	0.6(1)	1.2(3)	5	4217.3(8) ^f	5(1)	12(2)	1.1(1)	0.9(2)	1
						4239.1(3) ^a	14(2)	26(3)	0.0(1)	1.0(1)	6

^a No observed transition to the first excited state.

^b New parity assignment for previously-observed state.

^c $M1$ transition at 2287 keV [32] is reassigned by the present work as a transition to the first excited state.

^d Both a transition to the ground state and to the first excited state are observed at this energy.

^e Previously measured at $E_\gamma = 3809$ keV with $\Gamma_0 = 1.6$ meV [33]. New width is $\Gamma_0 = 41(7)$ meV.

^f Previously measured at $E_\gamma = 4217$ keV with $\Gamma_0 = 1.6$ meV [35]. New width is $\Gamma_0 = 25(6)$ meV.

Zilges *et al.* [36] compiled the R_{exp} values of about 170 levels in rare-earth nuclei and plotted the frequency distribution of these ratios. Two maxima, one at $R = 1/2$ and one at $R = 2$, are observed, thus showing that a large fraction of the rare-earth nuclei follow the Alaga rules. For comparison, the nonzero R_{exp} values of about 160 levels from ^{232}Th [21], ^{235}U [20], ^{236}U [37], ^{238}U [5], and the present work were collected and are shown in Figure 7. The most prominent distinction between the rare-earth and actinide nuclei is the maximum of $K = 0$ states which is not observed for the actinides. In both rare-earth and actinide nuclei, there is a large number of R_{exp} values between $1/2$ and 2. This is evidence of the K -mixing which is known to increase in regions of large level density [38].

Also, Zilges *et al.* [39] calculated the spreading widths

from averaged mixing matrix elements for rare-earth and actinide nuclei and compared them with widths extracted from isobaric analog resonances [40]. In Ref. [39], the spreading width for ^{238}U , ~ 8 keV, grossly underestimated the one from the isobaric analog state, 142(37) keV. However, substituting for the present work's $E1$ strength, the spreading width increases from ~ 8 keV to 133(30) keV, which agrees with the isobaric analog resonance width within the range of their uncertainties.

Weak, unresolved transitions can be observed at all energies within the continuum and their background-subtracted, relative intensities can be extracted. Using narrow $\Delta E = 50$ keV energy bins around the beam energy centroid E_{beam} within a $E_{beam} \pm 2\Delta E$ window, the I_s -weighted asymmetry \bar{A}_{HV} and transition strengths are determined for each of the four energy

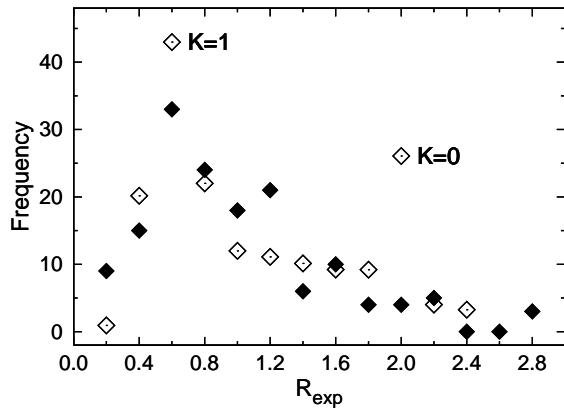


FIG. 7: The frequency distribution of R_{exp} values for the discrete transitions in rare-earth nuclei (\diamond) from Ref. [36] and in actinide nuclei (\blacklozenge) from the present work and Ref. [5, 20, 21, 37].

bins at all thirty beam energies between 2.0 - 6.2 MeV. An average R_{exp} for each of the bins is assumed to be the same as observed for discrete transitions.

The results are given as averages over 0.2-MeV wide energy bins in Fig. 8, where transition intensities contain both discrete and unresolved transitions. As the beam energy increased above 2.7 MeV, \bar{A}_{HV} decreased, denoting an increase in $E1$ strength. However, in the energy range $4.5 \geq E_\gamma \geq 6.2$ MeV, \bar{A}_{HV} values are only slightly negative, indicating similar intensity of unresolved $M1$ and $E1$ transitions. Alternatively, the average R_{exp} value may not well-represent the one for unresolved transitions such that transitions to the first excited state could prevail over those to the ground state. Fortunately the observation of a zero asymmetry at higher energies would still be observed under these conditions, regardless of the dominance of $E1$ transitions from the low-energy tail of the GDR.

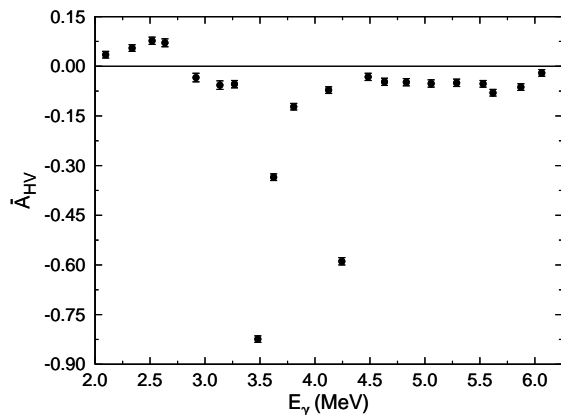


FIG. 8: The I_s weighted asymmetry \bar{A}_{HV} of the discrete and unresolved transitions for all 30 incident beam energies. Each point corresponds to an average asymmetry over a 0.2-MeV wide energy bin.

V. DISCUSSION

A. $M1$ Excitations

In the present measurement, $M1$ excitations are observed at approximately $2.0 \text{ MeV} < E_\gamma < 3.5 \text{ MeV}$ with a strong concentration of $M1$ states around 2.5 MeV. As E_γ increases, the $M1$ strength decreases until no more discrete states (above the lowest detection limit of about 3 eVb) are observed above 3.5 MeV. The upper limit of the integrated cross section of a $M1$ transition to the ground-state between $3.5 \text{ MeV} < E_\gamma < 4.2 \text{ MeV}$ is estimated to be 1 eVb. For incident-beam energy in the range of 2.0 - 4.2 MeV, $\Sigma B(M1)$ is found to be $8(1) \mu_N^2$ with ω_{M1} of 2.6(6) MeV for the observed $M1$ transitions.

The observed $M1$ strength may include states from both the scissors mode and the spin-flip mode, which are indistinguishable from each other based exclusively on the use of the NRF technique. A combination of theoretical models and experimental data from reactions other than (γ, γ') are needed for firm identification. The authors of Ref. [4] used a reformulation of the two-rotor model [41, 42] and the interacting boson model (IBA-2) [43] to determine the parameters for the scissors mode in ^{238}U . About two-thirds of the $M1$ strength found in the present measurement is observed in this range doubling the previous experiment's value of $3.2 \mu_N^2$ [4]. The observed strength is also about twice of the value measured for rare-earth nuclei [6].

The remaining amount of the total $M1$ strength, observed at energies above the scissors mode range, is about one-half of the value found in similarly deformed rare-earth nuclei [10], and only one-fifth of the spin-flip strength for ^{238}U measured by a (p, p') experiment [9]. The ω_{M1} for ^{238}U is similar to the observed 2.5 MeV in ^{232}Th [21] and ~ 3 MeV in many rare earth nuclei. One should note that the calculation of Ref. [44] for ^{238}U extends the scissors mode energy range to 4 MeV and pushes the spin-flip mode to 5 - 6 MeV. Due to the lack of any definitive theoretical models and the deficient comparisons with (e, e') reaction data over the same energy range, it can not be established which prediction for the scissors mode energy range is correct.

B. $E1$ Excitations

Most of the $E1$ transitions observed are above 3 MeV in excitation energy. As E_γ increased, the number of $E1$ states and the $E1$ strength increased due to the increasing proximity to the GDR. Multiple concentrations of states centered around the energies 3.1, 3.5, and 4.1 MeV are observed. For the energy range of 2.0 - 4.2 MeV, the observed $\Sigma B(E1)$ is $110(30) \times 10^{-3} e^2 \text{fm}^2$ with ω_{E1} of 3.3(8) MeV. For comparison, the $E1$ strength found in similarly deformed ^{154}Sm is $53 \times 10^{-3} e^2 \text{fm}^2$ [45].

An enhanced $E1$ strength above the extrapolated GDR tail could arise from octupole deformations or from α -clustering, two mechanisms discussed by Iachello in Ref. [46]. The octupole deformation is typically thought to be the origin of tran-

sitions existing in the energy range between 1 - 2 MeV. The octupole $E1$ strength can be estimated for this mechanism by the following equation [47]:

$$B(E1)_{oct} = \frac{9}{4\pi} \langle D_{oct}^2 \rangle, \quad (12)$$

where D is the electric dipole moment given as

$$D_{oct} = 6.87 \times 10^{-4} AZ\beta_2\beta_3 [e \text{ fm}], \quad (13)$$

and β_2 (β_3) is the quadrupole (octupole) deformation parameter. Using the β values from RIPL-2 [48], $B(E1)_{oct}$ is deduced to be $16 \times 10^{-3} e^2 \text{ fm}^2$. Therefore, octupole deformations could possibly account for only a small fraction of all the $E1$ strength seen in the present work. The $E1$ strength due to α -clustering is thought to be an origin of transitions in the energy range of 2 - 3 MeV and is estimated by the following equation [47]:

$$B(E1)_\alpha = \eta^2 \frac{9}{4\pi} \frac{\langle D_\alpha^2 \rangle}{6}, \quad (14)$$

where η is the clustering amplitude and D_α is given as

$$D_\alpha = 2e \frac{N-Z}{A} R_0 \left((A-4)^{1/3} + 4^{1/3} \right), \quad (15)$$

in terms of the neutron number (N), the proton number (Z), and the mass number (A). In order to reproduce the experimental $E1$ strength of $B(E1) \approx 31 \times 10^{-3} e^2 \text{ fm}^2$ in ^{238}U in the range between 2 and 3 MeV, the amplitude must be $\eta = 0.12$ which would indicate that other states are mixing into the ground state. Additionally, most of the $E1$ transitions observed in this work are above 3 MeV.

With less than half of the observed $E1$ strength possibly contributed by these two mechanisms, the remaining strength could be a product of the low-energy tail of the GDR. If the observed strength of the present work exceeds that of the strength from the low-energy tail of the GDR, then a PDR may exist within ^{238}U . To evaluate this GDR-tail influenced strength, the NRF cross section is extracted from the continuum between 2.0 - 6.2 MeV. Assuming that only ground-state transitions would appear on the right-hand side of the beam profile, an integration window is created at each beam energy. This window started at E_{beam} and then extended one standard deviation toward the high-energy side of the beam profile, thus excluding transitions to the first excited state. The flux, associated with this window, is used to produce the total cross section values. The average R_{exp} is weighted by the $E1$ strength and extracted from Table II to be 1.0(2).

The average total γ -ray interaction cross section σ_{tot} for $E1$ transitions is calculated using the methods from Ref. [33] and from Ref. [51]. For a zero-spin ground state and a dipole excitation, the ratio of the elastic scattering cross section to σ_{tot} is 0.67(16) with no open nucleon channels. The quantity σ_{tot} is corrected for coherent scattering involving the following processes: Rayleigh scattering [52], nuclear Thomson scattering,

Delbrück scattering [53, 54], and coherent nuclear resonance scattering [55]. The coherent contribution to the total photon interaction cross section between 2.0 and 6.2 MeV ranged from 1 - 23% with Delbrück scattering dominating the other scattering processes.

To evaluate the energy dependence of the $E1$ cross section, both the modified double Lorentzian (MLO) and the standard double Lorentzian (SLO) functions were used to fit the $^{238}\text{U}(\gamma, tot)$ data of Ref. [50] which included both photoneutron and photofission reaction cross sections. The strength function, measured in MeV^{-3} , with free parameters describing the energy E_r , the amplitude σ_r , and the width Γ_r , is of the following form [48]:

$$\vec{f}_{MLO}(E) = \frac{8.7 \cdot 10^{-8} E}{1 - e^{-\frac{E}{T_f}}} \sum_{i=1}^2 \frac{\sigma_{r,i} \Gamma_{r,i}^2}{(E^2 - E_{r,i}^2)^2 + (E \Gamma_{r,i})^2}, \quad (16)$$

where T_f is the final state temperature which can be approximated by the effective temperature T_{eff} of the target [26] such that it is ~ 1.2 MeV for the MLO fit to the data of Ref. [50]. The strength function for the SLO fit is similar to Eqn. 16, but does not include the exponential term. The total cross section σ_{tot} is calculated from

$$\sigma_{tot} = 3 (\pi \hbar c)^2 E \vec{f}_{MLO}(E). \quad (17)$$

The results are shown in Fig. 9: the σ_{tot} for $E1$ transitions from the present work, the experimental $^{238}\text{U}(\gamma, \gamma')$ cross section data from 4.9 - 6.2 MeV [49], the experimental $^{238}\text{U}(\gamma, tot)$ cross section data [50], as well as the MLO and SLO fits to the GDR data of Ref. [50].

In the present work, a large amount of $E1$ cross section was observed between 2.0 and 6.1 MeV with a total strength of 394(78) mb. However, it is very similar to the the summed

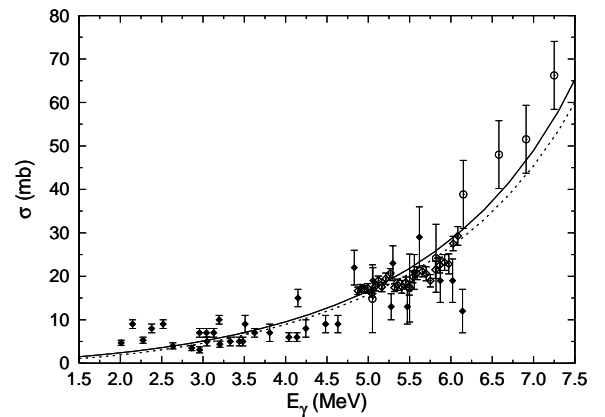


FIG. 9: The total γ -ray interaction cross section for $E1$ transitions from the discrete and unresolved transitions of the present work (\blacklozenge) compared with experimental $^{238}\text{U}(\gamma, \gamma')$ cross section data [49] (\diamond), and with $^{238}\text{U}(\gamma, tot)$ cross section data [50] (\circ). MLO fit (solid curve) and SLO fit (dashed curve) to the GDR [48, 50] are also shown.

TABLE III: $M1$ strengths for the observed discrete transitions in the present work compared with other experiments [4, 21, 37] and theoretical predictions [6, 17, 18] for actinide nuclei.

	Experiment					Theory						
	$^{232}\text{Th}^a$	$^{232}\text{Th}^b$	$^{236}\text{U}^c$	$^{238}\text{U}^b$	$^{238}\text{U}^d$	$^{232}\text{Th}^e$	$^{236}\text{U}^e$	$^{238}\text{U}^e$	$^{232}\text{Th}^f$	$^{236}\text{U}^f$	$^{238}\text{U}^f$	$^{238}\text{U}^g$
ω (MeV)	2.5	2.1	2.3	2.3	2.6(6)	2.5	2.6	2.6	2.6	2.6	3.2	-
$\sum B$ (μ_N^2)	4.3(6)	2.6(3)	4.1(6)	3.2(2)	8(1)	2.7(5)	5.4(2)	5.0(8)	5.0	6.1	8.3	6.0
$\sum B/\Delta E$ (μ_N^2/MeV)	2.2	5.2	2.9	5.3	3.5	2.7	5.4	5.0	2.5	3.1	2.3	1.5
Range (MeV)	2 - 4	1.9 - 2.4	1.8 - 3.2	2 - 2.6	2 - 4.3	2 - 3	2 - 3	2 - 3	2 - 4	2 - 4	2 - 5.6	2.6 - 6.6

^aRef. [21]. ^bRef. [4]. ^cRef. [37]. ^dPresent work. ^eRef. [6]. ^fRef. [17]. ^gRef. [18].

cross section produced from the MLO fit to the GDR, which has a cross section of about 400 mb in the same energy range. This observation is illustrated in Fig. 9 where σ_{tot} from the present work follows along the MLO and SLO fits without significant deviation. Therefore, no evidence is seen in the present data for the presence of a PDR in ^{238}U and all of the $E1$ strength observed is attributed to the low-energy tail of the GDR.

C. Comparison to theoretical calculations

The strengths of the dipole states observed in the present measurement are similar in magnitude to the strength predicted by the QRPA calculations in Refs. [17, 18]. Comparisons of experimentally summed strengths to the calculated values are given in Tables III and IV for even-even Th and for U isotopes. The summed $M1$ strengths from the present work and from the QRPA calculations [17, 18] have similar $\sum B/\Delta E$ whereas the previous experiment [4] and the sum rule predictions of Ref. [6] are larger by a factor of 1.5. The summed $E1$ strengths from the present work and from one of the QRPA calculations [17] have similar $\sum B/\Delta E$, although the second QRPA calculation from Ref. [18] is almost twice the $\sum B/\Delta E$ value from the present work.

The QRPA calculation by Kuliev *et al.* is fully renormalized and involves numerical calculations on ^{232}Th , ^{236}U , and ^{238}U in which the single-particle energies are obtained from Warsaw-deformed, Woods-Saxon potentials [17, 56]. The results, shown in Ref. [17], reproduce the gross structure of the present work's summed $M1$ and $E1$ strengths in this energy region fairly well. In Fig. 10, the calculations of Ref. [17] and the present work on discrete and unresolved transitions are compared using a 0.2 MeV bin size. Over half of the predicted $M1$ strength is present within 2.0 - 2.6 MeV and is assumed to be part of the scissors mode. Away from this narrow energy region, the predicted $M1$ strength decreases. Both of those features are observed in the present work. However, the $M1$ strength above 3.5 MeV is predicted with a similar amplitude as the transitions at lower energies. This feature is not observed in the present experiment.

Calculations of the $M1$ strength for the actinides by the authors of Ref. [17] yield a similar magnitude ($\sim 6\mu_N^2$), only underestimating the strength measured in this work by 25%. In the present work, eight $E1$ transitions are observed below 2.5 MeV of a summed strength equal to $20(4)\times 10^{-3}e^2\text{fm}^2$, which is much larger than predicted. The $E1$ strength calculations

do not predict the summed $E1$ strength well since there is significant strength above 4.3 MeV, which is not resolved in the experiment. Over 70% of the $E1$ strength predicted is located in the range between 4.3 and 5.6 MeV, and not at lower energies where a large amount of strength was observed.

Calculations by Soloviev *et al.* [18] were carried out using a quasiparticle-phonon nuclear model for ^{154}Sm , ^{168}Er , ^{178}Hf , and ^{238}U . The ^{238}U calculations predict two concentrations of dipole strength in the area of interest. One is a concentration of $M1$ strength between 2.6 - 3.0 MeV, and the second is a concentration of $E1$ strength between 3.4 - 4.0 MeV. In the present work, four concentrations are observed: one for $M1$ transitions around 2.5 MeV and three for $E1$ transitions around 3.1, 3.5, and 4.0 MeV.

The total $M1$ strength predicted by Ref. [18] and by Ref. [17] are similar in magnitude. The calculated $E1$ strength by Ref. [18] is about three times larger than the strength predicted by Ref. [17] as well as the value measured in the present work. Calculated $E1$ strength for rare-earth nuclei, which averages $\sim 250\times 10^{-3}e^2\text{fm}^2$ [18], is also larger than the experimental ^{238}U strength by a factor of two. Finally, it is found in Ref. [18] that the $E1$ strength is about 3-4 times larger than the $M1$ strength. In the present work, the observed $E1$ strength is only about 1.3 times larger than the $M1$ strength.

Lastly, Enders *et al.* [6] produced a calculation using a parameter-free "sum rule" to predict ω_{M1} and the $M1$ strength in the energy range of 2.0 - 3.0 MeV using the results of the Lipparini and Stringari analysis [57]. This "sum rule" prediction puts the range of the scissors mode between 2 and 3 MeV. This prediction agrees with the strength observed in the present work between 2 - 3 MeV. Also, these authors suggest that even though there is a possibility of scissors mode strength lying outside the region specified, it would only be a small fraction and no larger than the inherent uncertainty on the strength itself. Although a large portion of the $M1$ strength

TABLE IV: $E1$ strengths for the observed discrete transitions in the present work compared with experiments [21, 37] and theoretical predictions [17, 18] for even-even actinides.

	Experiment			Theory		
	$^{232}\text{Th}^a$	$^{236}\text{U}^b$	$^{238}\text{U}^c$	$^{232}\text{Th}^d$	$^{238}\text{U}^d$	$^{238}\text{U}^e$
ω (MeV)	3.7	2.5	3.3(8)	2.7	4.6	-
$\sum B \times 10^{-3}$ ($e^2\text{fm}^2$)	3.3(7)	6(1)	111(25)	35	120	308
$\sum B/\Delta E$ ($\times 10^{-3} e^2\text{fm}^2/\text{MeV}$)	2	4	48	18	33	77
Range (MeV)	2 - 4	1.8 - 3.2	2 - 4.3	2 - 4	2 - 5.6	2.6 - 6.6

^aRef. [21]. ^bRef. [37]. ^cPresent work. ^dRef. [17]. ^eRef. [18].

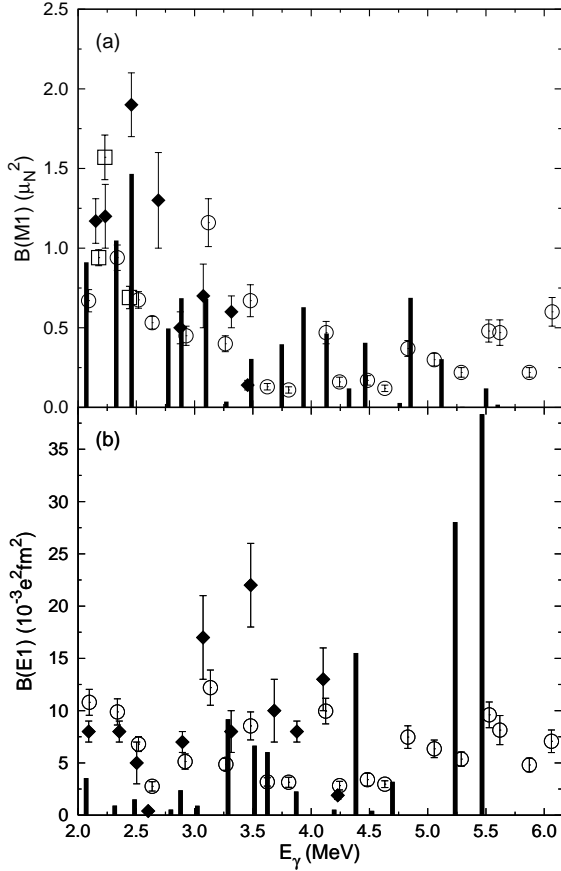


FIG. 10: Experimental (a) $M1$ and (b) $E1$ strengths (\blacklozenge) from the discrete transitions of the present work, (\circ) from the continuum of states of the present work, and (\square) from Ref. [4] are compared with a QRPA calculation (\circ) from Ref. [17] with a 0.2 MeV bin size. The strengths are shown with statistical error bars.

in the present work is contained in this specified region, a significant amount is observed at higher energies above 3 MeV.

VI. SUMMARY

NRF measurements were performed on ^{238}U at the HI γ S facility using 100% linear-polarized, quasi-monoenergetic

beams with energies between 2.0 and 6.2 MeV. One-hundred thirteen discrete deexcitations to the ground state at energies between 2.0 and 4.2 MeV are observed and their spin and parity are determined using the unique polarimetry setup of the detector array. Thirty percent of the observed states are $M1$ transitions and the rest are $E1$ transitions. Strengths as well as other spectroscopic data are measured for these states.

Above 4.2 MeV, only the asymmetry of the continuum of states could be investigated due to the detection limit of the experiment and the increasing level density. The average total γ -ray interaction cross section are determined from 2.0 to 6.2 MeV in order to deduce the origins of the low-lying strength. Comparison of the low-lying $E1$ strength to the MLO and SLO fits to the tail of the GDR provides evidence that this strength is not from a pygmy resonance. Discrete states are compared with QRPA calculations and “sum rule” predictions. These calculations and predictions describe the overall structure of the states but do not describe its finer details. More comparisons between experiments and theoretical calculations are needed for other rare-earth and actinide nuclei in order to provide a better understanding of the low-energy structure of nuclei with deformations and large neutron excess.

Acknowledgments

The authors would like to thank: LLNL, in particular M. S. Johnson and D. P. McNabb, for providing the ^{238}U targets; C. Huijbretgse, R. Raut, G. C. Rich, D. R. Ticehurst, and J. R. Tompkins for assistance in data taking and in technical discussions; and E. Guliyev for helpful explanations and discussions of QRPA calculations on ^{238}U . This work is supported in part by the Department of Homeland Security through the Academic Research Initiative with grants 2008-DN-077-ARI014 and 2008-DN-077-ARI010 and by the US Department of Energy with grants DE-FG02-97ER41041, DE-FG02-97ER41042, and DE-FG02-97ER41043.

[1] K. Heyde et al., *Rev. Mod. Phys.* **82**, 2365 (2010).
 [2] N. L. Iudice and F. Palumbo, *Phys. Rev. Lett.* **41**, 1532 (1978).
 [3] N. Pietralla et al., *Phys. Rev. C* **58**, 184 (1998).
 [4] R. D. Heil et al., *Nucl. Phys.* **A476**, 39 (1988).
 [5] A. Zilges et al., *Phys. Rev. C* **52**, R468 (1995).
 [6] J. Enders et al., *Phys. Rev. C* **71**, 014306 (2005).
 [7] G. F. Bertsch et al., *Rev. Mod. Phys.* **55**, 287 (1983).
 [8] A. Richter, *Prog. Part. Nucl. Phys.* **34**, 261 (1995).
 [9] H. J. Wörtche, Ph.D. thesis, Technische Hochschule Darmstadt

(1994), (unpublished).
 [10] D. Frekers et al., *Phys. Lett.* **244B**, 178 (1990).
 [11] Y. Suzuki et al., *Prog. Theor. Phys.* **83**, 180 (1990).
 [12] A. P. Tonchev et al., *Phys. Rev. Lett.* **104**, 072501 (2010).
 [13] U. Kneissl et al., *J. Phys. G.* **32**, R217 (2006).
 [14] P. Adrich et al., *Phys. Rev. Lett.* **95**, 132501 (2005).
 [15] F. Dönau et al., *Phys. Rev. C* **76**, 014317 (2007).
 [16] G. Rusev et al., *Phys. Rev. C* (R) **79**, 061302 (2009).
 [17] A. A. Kuliev et al., *Eur. Phys. J. A* **43**, 313 (2010).

- [18] V. G. Soloviev et al., *J. Phys. G* **25**, 1023 (1999).
- [19] H. R. Weller et al., *Prog. Part. Nucl. Phys.* **62**, 257 (2009).
- [20] E. Kwan et al., *Phys. Rev. C* **83** (R), 041901 (2011).
- [21] A. S. Adekola et al., *Phys. Rev. C* **83**, 034615 (2011).
- [22] N. Pietralla et al., *Phys. Rev. Lett.* **88**, 012502 (2002).
- [23] J. Apostolakis et al., *GEANT - Detector Description and Simulation Tool, CERN Program Library Long Writeup W5013*, CERN, Geneva, Switzerland (1993).
- [24] J. F. Briemeister, *Tech. Rep. LA-12625-M*, Los Alamos National Laboratory (1993).
- [25] W. Leo, *Techniques for Nuclear and Particle Physics Experiments (editor - W.D. Hamilton)* (Springer-Verlag, Berlin, 1994).
- [26] F. Metzger, *Prog. Nucl. Phys.* **7**, 53 (1977).
- [27] F. Ajzenberg-Selove, *Nucl. Phys.* **A506**, 1 (1990).
- [28] K. Debertin and R. Helmer, *Gamma- and X-Ray Spectrometry with Semiconductor Detectors* (North-Holland Pub. Co., Amsterdam, 1988).
- [29] J. Taylor, *An introduction to error analysis: the study of uncertainties in physical measurements* (University Science Books, 1997).
- [30] G. Alaga et al., *Mat. Fys. Medd. Dan. Vid. Selsk.* **29**, 1 (1955).
- [31] E. Hammarén et al., *Nucl. Phys.* **A541**, 226 (1992).
- [32] B. J. Quiter et al., *Nucl. Instr. Meth. B* **269**, 1130 (2011).
- [33] P. Rullhusen et al., *Nucl. Phys.* **A382**, 79 (1982).
- [34] W. Mückenheim and M. Schumacher, *J. Phys. (London) G* **6**, 1237 (1980).
- [35] U. Zurmühle et al., *Z. Phys. A* **314**, 171 (1983).
- [36] A. Zilges et al., *Phys. Rev. C* **42**, 1945 (1990).
- [37] J. Margraf et al., *Phys. Rev. C* **42**, 771 (1990).
- [38] T. Guhr et al., *Nucl. Phys.* **A501**, 95 (1989).
- [39] A. Zilges et al., *Z. Phys. A* **341**, 489 (1992).
- [40] J. Reiter and H. L. Harney, *Z. Phys. A* **337**, 121 (1990).
- [41] G. D. Franceschi et al., *Phys. Rev. C* **29**, 1496 (1984).
- [42] D. R. Bes and R. A. Broglia, *Phys. Lett.* **137B**, 141 (1984).
- [43] P. V. Isacker, *Phys. Lett.* **144B**, 1 (1984).
- [44] R. Nojarov et al., *Nucl. Phys.* **A563**, 349 (1993).
- [45] W. Ziegler et al., *Nucl. Phys.* **A564**, 366 (1993).
- [46] F. Iachello, *Phys. Lett.* **160B**, 1 (1985).
- [47] H. Friedrichs et al., *Nucl. Phys.* **A567**, 266 (1994).
- [48] T. Belgya et al., *Handbook for calculations of nuclear reaction data, RIPL-2*, IAEA, Vienna, Austria (2006).
- [49] Y. Birenbaum et al., *Phys. Rev. C* **36**, 1293 (1987).
- [50] J. T. Caldwell et al., *Phys. Rev. C* **21**, 1215 (1980).
- [51] P. Axel et al., *Phys. Rev. C* **2**, 689 (1970).
- [52] L. Kissel et al., *Phys. Rev. A* **22**, 1970 (1980).
- [53] P. Papatzacos and K. Mork, *Phys. Rep.* **21**, 81 (1975).
- [54] P. Papatzacos and K. Mork, *Phys. Rev. D* **12**, 206 (1975).
- [55] M. Schumacher et al., *Nucl. Phys. A* **346**, 418 (1980).
- [56] A. A. Kuliev et al., *J. Phys. G* **30**, 1253 (2004).
- [57] E. Lipparini and S. Stringari, *Phys. Rev. Lett.* **63**, 570 (1989).